Journal of the Optical Society of Korea, Vol. 6, No. 3, September 2002, pp. 59-71

Low-threshold Photonic Crystal Lasers from InGaAsP Free-standing Slab Structures

Han-Youl Ryu*, Se-Heon Kim, Soon-Hong Kwon, Hong-Gyu Park, and Yong-Hee Lee

Department of Physics, Korea Advanced Institute of Science and Technology, Daejon 305-701, KOREA

(Received May 9, 2002)

Photonic band gap structures have a high potential for nearly zero-threshold lasers. This paper describes new-types of low-threshold photonic crystal lasers fabricated in InGaAsP slab waveguides free-standing in air. Two-types of photonic crystal lasers are studied. One is a single-cell nano-cavity laser formed in a square array of air holes. This photonic band gap laser operates in the smallest possible whispering gallery mode with a theoretical Q >30000 and exhibits low threshold pump power of 0.8 mW at room temperature. The other laser does not have any cavity structure and the lasing operation originates from the enhanced optical density of states near photonic band edges. A very low threshold of 35 μW (incident pump power) is achieved from this laser at 80 K, one of the lowest values ever reported. This low threshold is benefited from low optical losses as well as enhanced material gain at low temperature.

OCIS codes : 140.3410, 140.3460, 140.5960, 160.4760, 220.4000.

I. INTRODUCTION

Advances in semiconductor processing technology have resulted in semiconductor micro-lasers with dimensions approaching a wavelength of the emitted light [1–4]. In the small optical cavities, lasers with ultra-low threshold and low operating power can be realized. These small, low power lasers integrated in dense arrays will be potentially used in high-speed optical connections and display applications with greatly reduced heat production. A figure of merit for the micro-cavity laser is a spontaneous emission factor (β) that is defined as the fraction of spontaneous emission coupled into the lasing mode. When β = 1, the laser will operate without threshold [1]. VCSELs (vertical-cavity surface-emitting lasers) [5] and micro-disk lasers [6,7] are good examples of micro-cavity lasers having small-size optical cavities and low threshold. However, βs in these lasers are not sufficiently small, typically less than 0.1 since the optical loss in these structures increases rapidly as the cavity size decreases.

Another optical cavity for strong photon confinement can be realized by employing photonic crystal structures, multi-dimensional periodic optical structures whose periodicity is on the order of the wavelength of light [8–10]. Photonic crystals can create a range of forbidden frequencies for spontaneous emission called a photonic band gap [11]. A resonant mode with $\beta = 1$ can be obtained in three-dimensional (3D) photonic crystals by coupling all spontaneous emission into the only existing resonant mode. However, fabrication of 3D photonic crystals still remains a great technological challenge. A relatively simple way to achieve strong 3D photon confinement is to combine a two-dimensional (2D) photonic crystal with a slab waveguide [12,13]. This photonic crystal slab structure is composed of an optically thin dielectric slab surrounded by air or low-index materials for vertical confinement and a 2D photonic crystal for in-plane confinement of light. A large β ~0.8 has been theoretically predicted in the photonic crystal slab single-cell cavity mode whose dimension is only a few times $(\lambda/2n)^3$, where λ is the emission wavelength and n is the refractive index [14].

Recently, 2D photonic crystal lasers have been demonstrated by several groups [15–27]. There have been two types of such lasers. The first one has a resonant cavity formed by introducing local defect structures in a periodic photonic lattice and lasing actions arise from the resonant cavity modes [15–20]. Photonic crystal single-cell lasers were reported from triangular lattices of air-hole structures free-standing in air [15,16,20]. The second type of photonic crys-

tal lasers does not have any physically-defined cavity [21,23–27]. The operation of this laser is based on the enhancement of optical density of states at photonic band edges [28,29]. This photonic band edge laser is a 2D analogue of the one-dimensional distributed feedback laser [30]. However, threshold in reported photonic crystal lasers has not been very low. Even in a single-cell laser, the threshold pump power was larger than 1 mW [15,16]. This relatively large threshold partly originates from the low quality factor (Q) of the resonant mode. The Q of the previously reported triangular lattice single-cell laser mode was only several hundred [13,16]. Therefore, in order to achieve much reduced threshold, it is necessary to create a high-Q resonant mode in the wavelength-size single cell cavity. For photonic band edge lasers, the periodic refractive index variation (Δn) has been very small, typically on the order of 0.1, which resulted in large active area and high threshold [23–27]. In order to achieve low-threshold photonic band edge lasers, Δn should be increased by a large amount.

In this paper, experimental results and theoretical analyses on low-threshold photonic crystal lasers are presented. Laser structures are fabricated in free-standing InGaAsP slab waveguides emitting at 1.4 μm $\sim$ 1.6 μm. Both types of photonic crystal lasers, single-cell lasers and band edge lasers, are studied. By employing new-types of photonic crystal geometry, the thresholds of these lasers are much reduced from previous results on photonic crystal lasers. Interesting characteristics are observed from these newly investigated lasers.

As an effort to achieve a high-Q single-cell resonant mode, square lattice photonic crystal structures are investigated. It will be addressed later that a very high-Q resonant mode is realized in this single-cell nano-cavity, and low-threshold lasing operation is also demonstrated by room-temperature optical pumping. Photonic band edge lasers fabricated in the free-standing slab have large Δn since the air-hole patterns are entirely transferred through the slab. Large Δn results in small device size and low threshold due to strong enhancement of optical density of states near photonic band edges. Since, the active area is only a few μms, the band edge laser operates in a single mode with a high β and low threshold. One of the record low-threshold pump powers is achieved from this laser at 80 K.

II. DESIGN AND FABRICATION

The schematic diagram of a free-standing photonic crystal slab with a square lattice single-cell cavity is shown in Fig. 1(a). Multiple quantum well active layers are positioned in the middle of the slab. There are several structural parameters such as slab thickness, lattice constant, air-hole radius, and refractive index of the slab material, which determine optical properties of the photonic crystal slab such as a band structure, resonant modes, and the Q of the mode. In the calculation of the band structure, the plane-wave method with conjugate gradient minimization algorithm is used [31,32]. Due to the complex geometry, a full 3D calculation is performed. The resonant frequencies, mode profiles, and Qs are calculated by using the 3D finite-difference time-domain (FDTD) method with perfectly matched layer boundary conditions [13,33]. In the FDTD calculation, computational space steps are 15 intervals per lattice constant. In all calculations, the refractive index of the slab material is chosen to be 3.4, which corresponds to the refractive index of InGaAsP at 1.55 μm. Based on the calculation results, the design parameters of photonic crystal lasers are determined and applied to fabrication processes.

Fabrication procedure for a free-standing photonic crystal slab structure is shown in Fig. 1(b). Seven pairs of strain-compensated InGaAsP quantum wells are used as the active material. These materials are frequently employed in photonic crystal light-emitting structures mainly due to relatively small surface recombination [15–22].

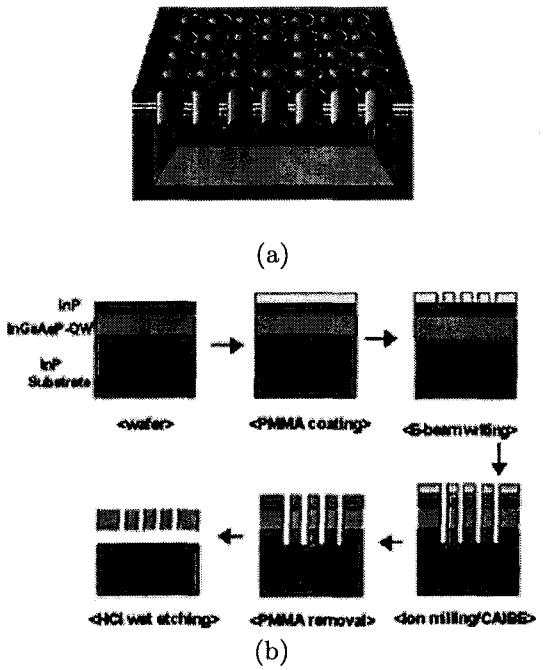

FIG. 1. (a) Schematic diagram of a free-standing photonic crystal slab with square lattice single-cell cavity. In this figure, three quantum-wells are positioned inside the slab. (b) Fabrication procedure for free-standing photonic crystal slab structures.

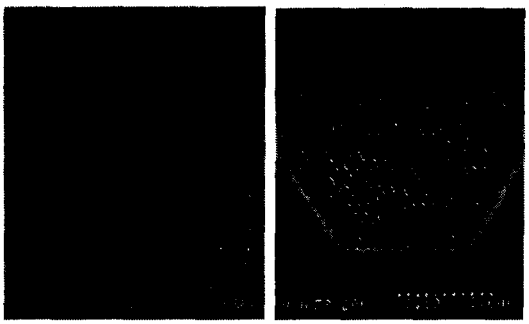

(a) (b)

FIG. 2. Top-view scanning electron micrograph of fabricated photonic crystal slab laser structures. The thickness of the InGaAsP free-standing slab is 200 nm. (a) Square lattice single-cell cavity laser. Lattice constant (a) is about 525 nm and air-hole radius (r) is 0.38 a. (b) Photonic crystal band edge laser. a is 1000 nm and r is 0.35 a.

First, PMMA (poly-methyl methacrylate) is coated on a InP/InGaAsP wafer. Then, 2D photonic crystal patterns were formed by using electron-beam lithography. After developing, the patterns are transferred through the wafer by Cl_2-assisted Ar-beam etching at 250 °C. The patterned layer was then separated from the InP substrate to leave a free-standing slab by use of wet etching with diluted HCl solution. The thickness of the InGaAsP slab is 200 nm. Top-view scanning electron micrographs of fabricated free-standing photonic crystal slabs are shown in Fig. 2. A square lattice single-cell laser structure and a photonic band edge laser structure are shown in (a) and (b), respectively.

III. SQUARE LATTICE PHOTONIC CRYSTAL SINGLE-CELL LASER

1. Motivation

Up to now, the triangular lattice of air holes has been a natural choice for photonic band gap lasers [15–18] due to the existence of a large TE photonic band gap. However, the dipole mode formed in the normal triangular lattice single-cell cavity has a relatively low Q, usually below 1,000 [13,16]. This is because the cavity loss of the slab-type 2D photonic crystal cavities is dominated by the radiation loss out of the slab [13,34] rather than the propagation loss in the photonic crystal plane. This implies that the consideration of vertical coupling should be more important than that of in-plane mode confinement by the photonic band gap. The relatively low Q of the dipole mode originates from the nature of dipole oscillation which emits radiation predominantly in the vertical direction [34,35]. Therefore, other lattice structures can also be good candidates for a photonic crystal single-cell laser if the resonant mode with low vertical losses can be found.

A micro-disk cavity offers a valuable insight into the low-loss high-Q modes to be achieved in the photonic crystal cavities. Whispering gallery modes formed by use of total internal reflection in the micro-disk cavity radiate mostly in the radial direction [6,36]. Due to the exponential decrease of the Q with decreasing disk size, it was difficult to realize lasing operations in the whispering gallery mode of the micro-disk with diameter smaller than 1.5 μm and the azimuthal mode number $<$5. If this radial radiation can somehow be suppressed, whispering gallery modes with high Qs and smaller mode numbers would be realized. In this sense, it is expected that, if the whispering-gallery-like modes can be formed in a photonic crystal slab cavity, these modes could have high Qs since both in-plane and out-of-plane radiation are suppressed at the same time.

It is interesting to note that the C_{4v} symmetry of 2D square lattice photonic crystals allows the existence of the whispering gallery mode with a lowest azimuthal mode number of 2. The square lattice single-cell cavity is an ideal structure to confirm the existence of this fundamental whispering gallery mode. In fact, square lattice air-hole photonic crystals have hardly been investigated because the size of the band gap for in-plane polarization (TE-polarization) is much smaller than that of the triangular lattice.

2. Resonant modes in the square lattice single-cell cavity

To start, 3D FDTD methods are used to calculate resonant frequencies, mode profiles, and Qs of single-cell cavity modes in a free-standing square lattice photonic crystal slab. A single-cell is introduced by removing one air hole in the periodic square lattice as appears in Fig. 2(a). The thickness of the slab is 0.4 a where a is periodicity of the square lattice.

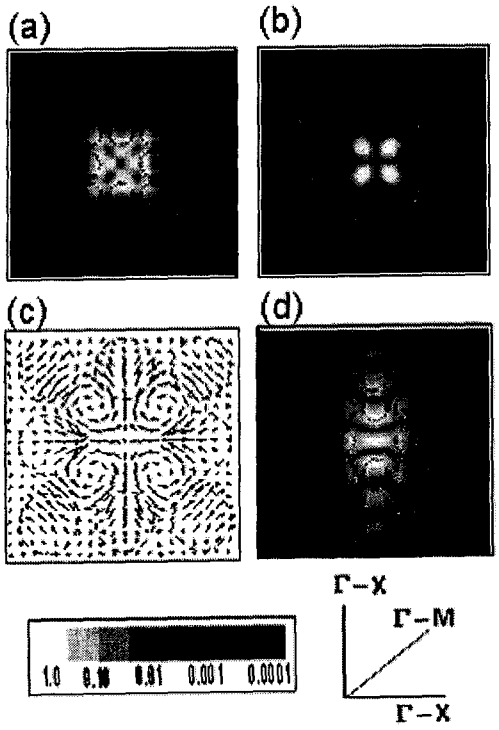

FIG. 3. Resonant mode profiles of a free-standing square lattice single-cell cavity. (a) Electric field intensity profile of the whispering gallery (WG) mode calculated at the center of the slab. (b) Magnetic field intensity profile of the WG mode. (c) Electric field directions of the WG mode. (d) Electric field intensity profile of the y-dipole mode. Dotted lines represent square lattice air-hole patterns. Γ-X and Γ-M crystalline directions of the square lattice are also shown.

Two types of resonant modes appear in this cavity. The first one is nondegenerate and has a square symmetry as shown in Figs. 3(a)~(c). The electric field and the magnetic field intensity profile are shown in Figs. 3(a) and (b), respectively. Electric field direction of this mode is also calculated and shown in Fig. 3(c).

Maximum intensity of electric fields exists around four nearest neighbor holes, whereas that of magnetic fields exists in the diagonal direction around the center. Both electric and magnetic fields have a node at the center. These features are reminiscent of the whispering gallery mode in the micro-disk cavity. In addition, electric fields at four intensity maxima are directed radially in and out alternatively, which is also characteristic of the lowest-order whispering gallery mode (WG) with the azimuthal mode number of 2.

The other resonant mode is the dipole mode which is doubly degenerate. The electric field intensity profile of the dipole mode which oscillates in the y-direction is shown in Fig. 3(d), and the other dipole mode oscillates in the x-direction.

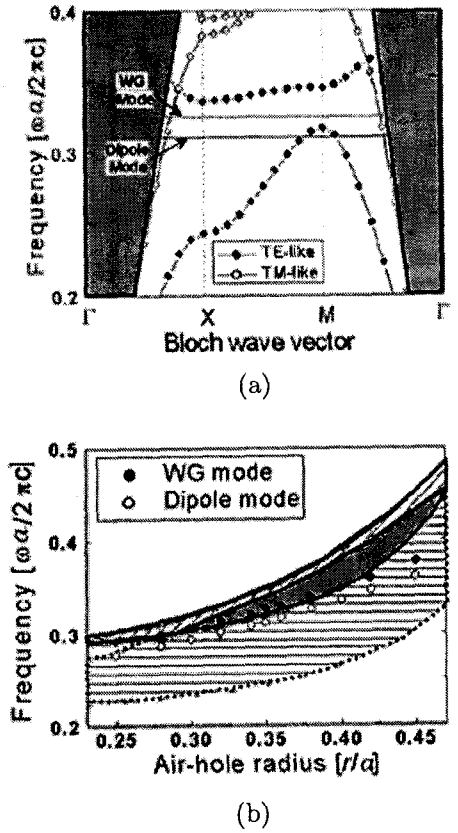

FIG. 4. (a) Band structure of a free-standing square lattice for $r = 0.35\ a$. Slab thickness is 0.4 times the lattice constant of the square lattice ($d = 0.4\ a$). Modes above light lines (gray region) are leaky and couple to free space. (b) Resonant frequencies and band gap positions as a function of air-hole radius. Gray area represents a full in-plane band gap region. Horizontally and obliquely hatched areas below and above the gray area indicate the band gap in the Γ-X and the Γ-M direction, respectively.

Resonant frequencies and Qs of both cavity modes are calculated varying the radius of air holes. First, the band structure of a square lattice photonic crystal slab is shown in Fig. 4(a) when the air-hole radius is 0.35 a. A narrow band gap of TE guided modes appears. Resonant frequencies of each mode are represented by horizontal lines. In this case, the WG mode exists inside the in-plane TE band gap, whereas the dipole mode exists below the band gap. The resonant frequencies versus air-hole radius are plotted in Fig. 4(b) along with band gap positions. Gray area represents a full in-plane band gap frequency region. Hatched areas below and above the gray region indicate the band gap in the Γ-X direction and Γ-M direction, respectively. These crystalline directions are represented in Fig. 3. The resonant frequency of the WG mode is within the full band gap in most cases. However, it is interesting to note that the resonant fre-

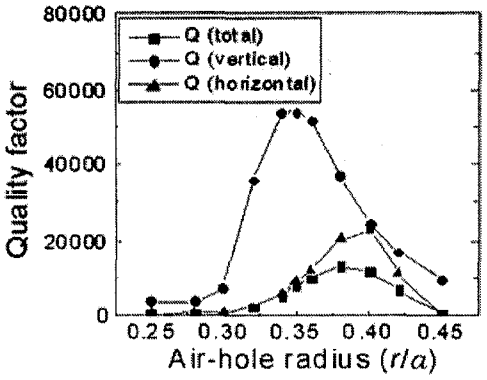

(a)

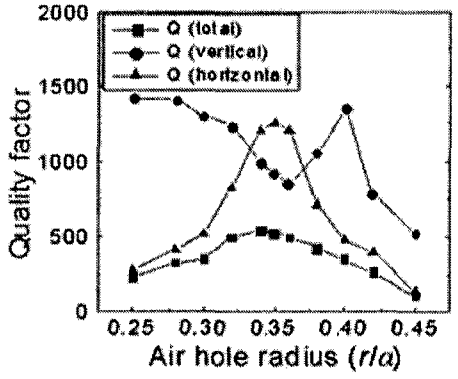

(b)

FIG. 5. Quality factors (Qs) are shown as a function of air-hole radius for the WG mode (a) and the dipole mode, respectively (b) Total Qs of each mode are decomposed into the horizontal Qs (solid circle) and the vertical Qs (solid triangle). 11×11 unit cells in the photonic crystal plane are employed for the calculation.

quency of the dipole mode lies outside the full in-plane band gap for all air-hole radii. This is because only the band gap for the Γ-X direction plays an important role, since the dipole modes oscillate predominantly in the Γ-X direction

The computational domain for Q calculations contains 11×11 unit cells in the photonic crystal plane. As shown in Fig. 5(a), the total Q of the WG mode are usually several thousand and the Q of about 13000 is observed when the air-hole radius is about 0.38 a. The total Q is decomposed into the vertical Q and the horizontal Q. The boundary for separating vertical radiation from laterally guided modes is positioned at approximately half-wavelength from the surface of the slab [13]. Considering that the Q of the resonant mode ultimately approaches the vertical Q since the horizontal Q increases exponentially as the computational domain size is enlarged [13], the Q of the WG mode can be as large as 50000. It will be shown later that the vertical Q can be even higher than 100000

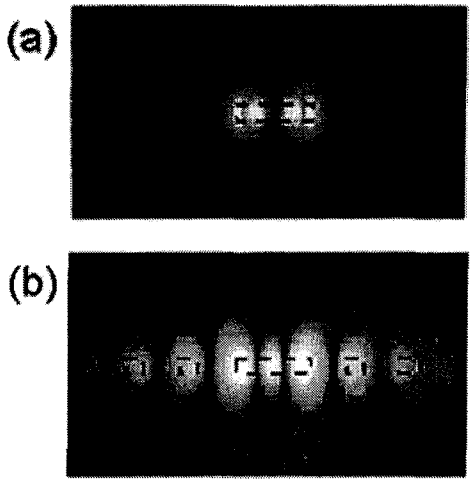

FIG. 6. (a) Side-view electric field intensity profile of the WG mode calculated along the Γ-X direction through the defect center. (b) Side-view electric field intensity profile of the dipole mode. Dotted lines represent the side-view of the square lattice single-cell slab structure.

when the square lattice slab single-cell cavity is optimized by changing the structural parameters. The calculated results support the previously mentioned argument that the mode with whispering-gallery-like profiles will have a high Q in the photonic crystal cavity. In the micro-disk cavity, such high Q values of the lowest order WG mode cannot be addressed due to significant radiation losses. So, the above results imply that the photonic band gap is more effective than total internal reflection for photon confinement in wavelength-size micro-cavities.

The Qs of the dipole mode are smaller than those of the WG mode by more than an order of magnitude. The largest Q obtained for the dipole mode is only about 550 as shown in Fig. 5(b). These Q values are similar amount to those of the dipole mode in the triangular lattice single-cell structure [13,16]. Considering that the dipole modes of square lattice air-hole structures are formed outside the in-plane band gap, it is remarkable that the Qs of dipole modes are comparable to the triangular lattice cases. Figs. 6(a) and (b) show the side view of electric field intensity profiles for the WG and the dipole mode, respectively. The electric field of the WG mode is well confined inside the slab. Note especially the large difference of vertical coupling between two modes.

3. Experimental results on room-temperature lasing

The square lattice single-cell structures were optically pumped by a 980-nm laser diode with 10 ns

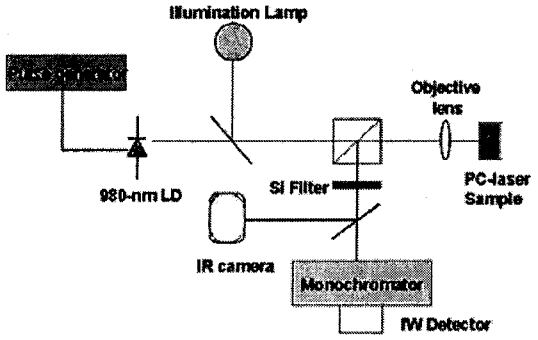

FIG. 7. Measurement setup for the optical characterization of photonic crystal (PC) lasers.

pulses at a repetition rate of 500 kHz. The pump spot size was about 3.5 μm. Emitted light was collected from the top of a sample using a microscope objective with a numerical aperture of 0.85. All experiments were performed at room temperature. The measurement setup is shown in Fig. 7.

Lasing actions are observed from many samples with various lattice parameters. Lasing from both the WG mode and the dipole mode was observed and identified. The characteristics of the WG mode laser with lowest threshold are summarized in Fig. 8. This laser structure corresponds to the sample shown in Fig. 2(a). The mode profile of the WG laser is taken from an infrared camera and shown in the inset of Fig. 8(a). The mode image clearly shows a four-lobe shape and a nodal point at the center, which is characteristic of the lowest-order whispering gallery mode. Each laser mode is also identified by polarization measurements. The dipole mode is nearly linearly polarized, whereas the WG mode does not have definite polarization directions.

From the L-L (light-out versus light-in) curve shown in Fig. 8(a), the threshold peak pump power is estimated to be about 0.8 mW for the WG mode laser. The threshold of the triangular lattice single-cell laser was 1.5 mW [16]. Therefore, the measured threshold is almost two times lower than the previous result. The lowest threshold of the dipole mode laser of the square lattice is about 1.0 mW, which is 20% higher than that of the WG mode laser. This reflects the higher Q of the WG mode. Considering that Qs of the WG mode can be more than 10 times higher than those of the dipole mode, the measured threshold of the WG mode is not much reduced. This is because the threshold of a photonic crystal single-cell laser is limited by absorption in the mirror region, transparent carrier density, and carrier losses due to diffusion and nonradiative recombination. Due to the quantum-well absorption in the mirror region, the pumping area is much larger than the mode size to compensate absorption losses. The pumping area is about 30 times larger than the

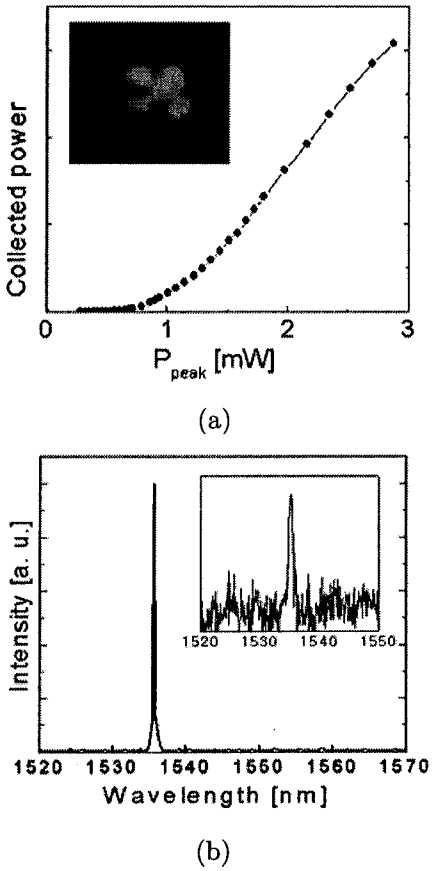

FIG. 8. Characteristics of the WG mode single-cell laser shown in Fig. 2(a). (a) Collected output power measured at the lasing wavelength is plotted as a function of peak pump power (L-L curve). The infrared camera image of the laser mode profile is shown in the inset. (b) Laser spectra measured at the peak pump power of 5 mW. The photoluminescence spectra measured at 0.4 mW are shown in the inset. Linewidth of spectra is limited by the resolution of the spectrometer.

cavity area. Therefore, if there was no absorption in the mirror region and pumping was performed only in the cavity region, threshold less than 30 μW could be achieved. Assuming 20% of pump power is absorbed in active regions, this threshold value roughly corresponds to about 5 μA in the case of electrical pumping, which corresponds to the lowest threshold value ever reported.

Emission wavelength of this best WG laser is 1.535 μm near the gain peak of InGaAsP active materials. To determine the Q of the mode experimentally, the spectral linewidth of the single-cell mode is measured near the transparency pumping condition. The inset of Fig. 8(b) shows the spectrum of the WG mode when the pump power is 0.4 mW. From the measurement of full-width at half maximum, the Q of the WG mode is estimated to be about 2000. This Q value is

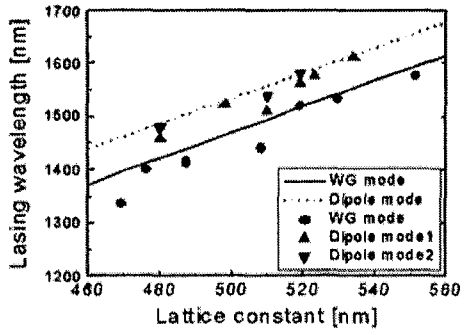

FIG. 9. Plots of lasing wavelengths as a function of lattice constants of samples. The air-hole radius of all samples is 0.38 a. Dot symbols and lines represent measured wavelengths and 3D FDTD simulation results, respectively. Lasers from two split dipole modes are also observed and lasing wavelengths are plotted.

limited by the resolution of the spectrometer. The measured Q compares reasonably well with the previous calculation results.

In Fig. 9, measured laser wavelengths are plotted and compared with calculated resonant wavelengths as a function of lattice constants when the air-hole radius is 0.38 a. Dot symbols represent the experimental values and lines are the calculated results obtained from 3D FDTD calculations. Lasing actions in a wide spectral range between 1340 nm and 1610 nm are obtained. Considering fabrication inaccuracy, the agreement between calculation and measurement is good. Lasing actions from two split dipole modes are observed in several samples. The amount of the splitting is about 2% which is well within the fabrication tolerance. No splitting of the emission wavelength from the WG mode is observed, which indicates that the WG mode is truly nondegenerate.

4. Prospect of the whispering gallery mode in the square lattice single-cell cavity

The WG mode of a square lattice single-cell cavity has several unique and advantageous features. First, this mode has a very high Q and small mode volume. This mode has demonstrated a spectrometer-limited below-threshold Q >2000 and a theoretical total Q of >10000 in the previous sections. The Qs can be increased further by changing the structural parameter. In Fig. 10(a), the total, vertical, and horizontal Qs of the WG mode are plotted as a function of slab thickness. In this calculation, the computational domain is increased to 13×13 unit cells and the air-hole radius is fixed to 0.38 a. The vertical Q increases with slab thickness, and is even higher than 100000 when the

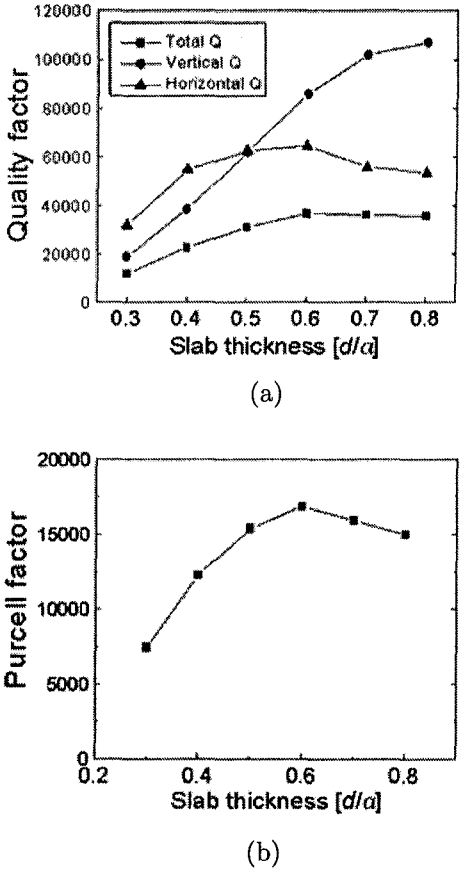

FIG. 10. Quality factors (a) and the Purcell factors (b) as a function of slab thickness. The air-hole radius is fixed to 0.38 a. The total Q is decomposed to the vertical and the horizontal Q in (a).

slab is thicker than 0.7 a. The horizontal Q has a maximum when the slab thickness is around 0.6 a due to the appearance of higher order guided modes [32]. At this slab thickness, the total Q of 37000 is obtained. These calculated Qs are the largest Qs of the single-cell cavity mode ever reported. In addition to the Qs, the WG mode has wavelength-size small mode volume. The calculated effective mode volume is about 0.04 μm^3 which approximately corresponds to 3.5 $(\lambda/2n)^3$. Here, the effective mode volume is defined as the ratio of total electric field energy to the peak value of electric field energy density [15,16]. The large Q and the small mode volume results in strong enhancement of spontaneous emission [37,39]. The theoretical enhancement is given by the Purcell factor F_p [12],

$$F_p = \frac{Q}{4\pi V_{eff}} \left(\frac{\lambda}{n_{eff}}\right)^3, \quad (1)$$

where Q, V, n_{eff}, and ν are a quality factor, mode volume, effective refractive index, and resonant frequency, respectively. Using the parameters calculated

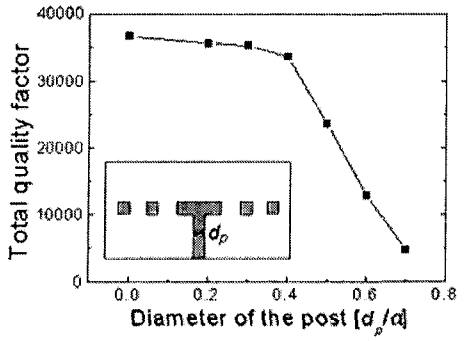

FIG. 11. Total Qs as a function of the diameter of the electrical post. The schematic diagram of the post structure is shown in the inset. The air-hole radius and the slab thickness are 0.38 a and 0.6 a, respectively.

by the 3D FDTD, the Purcell factor is plotted as a function of slab thickness in Fig. 10(b). The Purcell factor can be larger than 10000. This is the largest value of reported Purcell factors. Therefore, it is expected that the WG mode can offer great opportunities to study cavity quantum electrodynamics in micro-cavities.

The WG mode has other favorable properties for photonic crystal micro-cavity devices. The nondegeneracy of this WG mode will result in a large spontaneous emission factor [14], which implies that this mode has a high potential for the realization of a thresholdless laser. And, since there is an intensity node at the center of the cavity, electrical pumping can be achieved without degrading mode properties by placing a current flow path at the cavity center as has been realized in the micro-disk lasers. In Fig. 11, the total Q is plotted as a function of the diameter of the post positioned under the center of the single-cell cavity. The total Q is still over 30000 until the post diameter reaches 0.4 a, This result implies the possible application of electrical pumping to the WG mode.

IV. FREE-STANDING PHOTONIC CRYSTAL SLAB BAND EDGE LASER

1. Motivation

Several photonic band edge lasing operations have been experimentally demonstrated by using semiconductor [23,27] or organic materials [24–26]. Some interesting features have been observed such as 2D feedback mechanisms [25], saddle point lasing [26], and mirrorless lasing. In all these previous demonstrations of band edge lasing actions, however, the periodic refractive index variation Δn has been very small. As a result, the active area was larger than (100 μm)^2 to achieve sufficient gain to reach the lasing threshold. Consequently, the threshold in previous photonic band edge lasers has been somewhat large.

In this work, photonic band edge lasers formed in a free-standing photonic crystal slab are demonstrated. Since the air-hole patterns are entirely transferred through the slab, Δn of the structure is >2 which is more than ten times larger than that of the previous band edge lasers. Theoretical investigation has predicted that the threshold of band edge lasers will decrease with Δn [28,29]. As Δn increases, bands near Brillioun zone edges become flatter. Then, the group velocity of photons becomes lower and threshold gain will be reduced. Sakoda et al. showed that threshold gain would be proportional to the square of the group velocity [29]. Another consequence of the large Δn is that the size of photonic band edge lasers can be made small. It has been shown by calculation that a small number of periodic arrays (~5) could produce significant light amplification [29].

In photonic band edge lasers, photons generated in the pumped area form quasi-standing wave patterns at band edges. So, the pump region itself functions as a cavity though no physically defined cavity and mirror structures exist. Therefore, the concept of a Fabry-Perot resonator can also be applied to this band edge laser. If an active area of the band edge laser is as small as a few μm^2, a single-mode operation can be obtained because of the large Fabry-Perot mode separation of the small cavity. In this sense, the free-standing photonic band edge laser is expected to show very low threshold lasing action.

2. Band edge lasing operation

The photonic band edge laser structures are fabricated by the methods described in the section II. The photonic crystal pattern is a triangular array of air holes patterned in the free-standing slab. The thickness of the InGaAsP slab is 200 nm as in the previous experiments. The lattice constant of samples is varied from 400 nm to 1200 nm. The size of each sample is about 20 μm. A top-view scanning electron micrograph of a fabricated structure has been presented in Fig. 2(b). In this sample, the lattice constant is 1000 nm and the air-hole radius is 0.35 a, where a is the lattice constant. In fact, this defect-free air-bridge slab structure is nearly identical to those investigated in several other works where emission characteristics or enhanced light extraction have been reported [39,40]. At room temperature, no lasing action is observed from this photonic crystal slab structure. At low temperature, however, very strong band edge lasing is achieved from the structure in Fig. 2(b). The realization of band edge lasing is ascribed to much

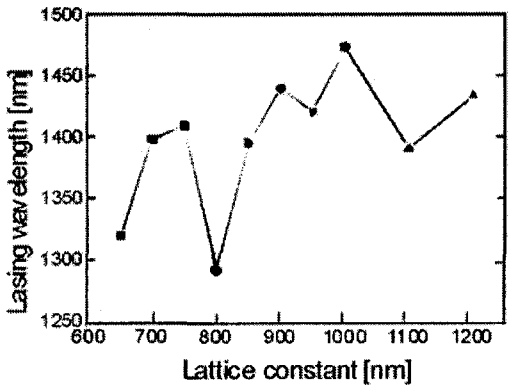

FIG. 12. Lasing wavelengths of photonic band edge lasers as a function of lattice constant. The air-hole radius is 0.35 a for all samples. It will be shown in Fig. 13 that square and circle symbols correspond to the second and the third TE mode band edge lasing, respectively. Triangular symbols corresponds to the TM mode band edge lasing.

reduced surface recombination carrier losses and increased material gain at low temperature.

The fabricated structures are pulse-pumped by a 980-nm laser diode. Samples are placed inside a liquid nitrogen cryostat and temperature is maintained at 80 K. Pump pulse width is 10 ns and duty cycle is 4%. The pump spot size is about 6 μm. This spot size is regarded as the active area. Typically, the pumping is performed at the center of the laser pattern. Emitted light is collected from the top of the sample by a $\times 20$ objective lens. Laser emissions from samples with various lattice parameters are observed.

When the lattice constant of samples is smaller than 600 nm, in-plane propagation of laser emission is observed, indicating that the lasing action originates from the band edges below the light line of a band structure. On the contrary, vertical emitting characteristics are observed when the lattice constant is larger than 600 nm. These vertical emitting lasing actions occur near the Γ point of bands above the light line of a photonic band structure [23,27]. Here, mainly vertical-emitting photonic band edge lasers are studied. The lasing wavelengths for the samples with lattice constant >600 nm are plotted in Fig. 12. The air-hole radius of the plotted samples is about 0.35 a. Lasing in a wide spectral range, 1290 nm $\sim$ 1480 nm, is observed. This is rather surprising because the emission linewidth of InGaAsP quantum wells at this temperature is much smaller than this spectral range. The FWHM (full-width at half-maximum) of photoluminescence is about 50 nm. Furthermore, most band edge laser samples show single mode lasing action in this wide wavelength range. The 6-μm active area corresponds to the free spectral range of 60 nm $\sim$ 70 nm which is larger than the FWHM. Therefore, the single mode operation is understandable. Consequently, these lasers will have large spontaneous emission factors. In Fig. 12, there is steep drop of the lasing wavelength at the lattice constant, 650 nm, 800 nm, and 1100 nm. Since the lasing wavelength usually increases with lattice constants in a given mode, this result indicates hopping to an other band edge mode.

In order to compare the experimentally observed lasing wavelengths with calculation, the photonic band diagram corresponding to the structure in Fig. 2(b) is calculated by using the three-dimensional finite-difference time-domain (FDTD) method [41,42]. Bloch and perfectly matched layer boundary conditions are used for the horizontal and the vertical boundary condition, respectively. In Fig. 13(a), the band structure for the TE (transverse electric) modes is plotted along the Γ-M direction of the triangular lattice. Three TE bands are plotted in this figure. The slab thickness and air-hole radius are 0.2 a and 0.35 a, respectively. The refractive index of the slab material is 3.4 as in the previous calculations. Modes below the light line are guided along the photonic crystal slab and modes above the light line usually couple out of the slab [31,32]. Consequently, modes above light lines are leaky and usually have low Qs. Therefore, it can be inferred that the band edge lasers operating near the Γ point undergo large optical losses and show poor laser characteristics. However, it will be shown later that some modes near the Γ point can have very high Qs and exhibit good lasing performances.

The calculated band edge frequencies at the Γ point are shown as a function of lattice constant in Fig. 13(b) for the air-hole radius of 0.35 a. Solid and dotted lines represent the TE and TM (transverse magnetic) mode, respectively. The measured wavelengths in Fig. 12 are converted to the units of the normalized frequency and plotted in Fig. 13(b) as solid dots. Square and circle symbols correspond to the second and the third TE mode band edge, respectively. For the samples with lattice constant >1 μm, lasing action seems to occur at TM mode band edges. The nonuniformity of air holes and the measurement errors of lattice parameters are partly responsible for the small discrepancy of calculated and measured data. The other reason is related to the fact that the Bloch wave vector k is not exactly defined due to the small active area. This means that the measured band edge lasing wavelengths do not exactly correspond to the Γ point.

3. Characteristics of the lowest-threshold band edge laser

The characteristics of a photonic crystal slab band

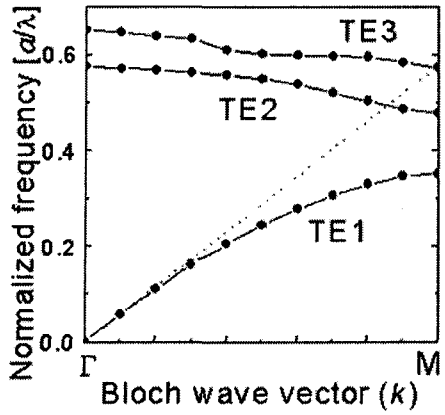

(a)

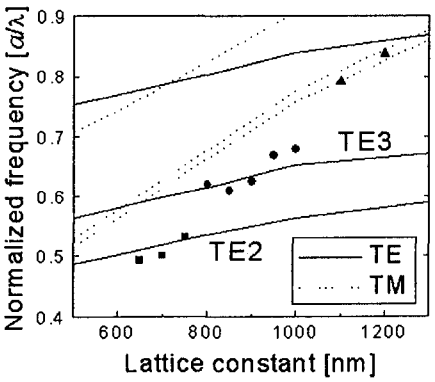

(b)

FIG. 13. (a) Band diagram of the structure in Fig. 2(b). Three TE bands along the Γ-M direction are shown. Dotted line represents the light line. (b) Measured wavelengths in Fig. 12 are converted to the unit of the normalized frequency and plotted as solid dots. Square and circle symbols correspond to the second and the third TE mode band edge, respectively. Triangular symbols corresponds to the TM mode band edge. Calculated band edge frequencies at the Γ point of the band diagram are also shown as solid and dotted lines.

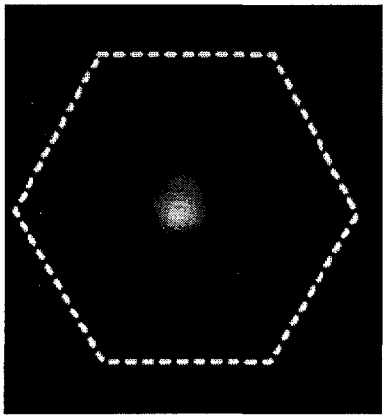

(a)

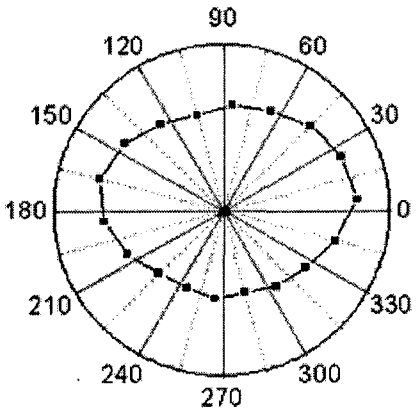

(b)

FIG. 14. Characteristics of a band edge laser sample with lattice constant of 1000 nm. (a) Mode pattern image taken by the infrared camera. A dotted hexagon represents the boundary of the photonic crystal laser pattern. (b) Polarization angle of this laser. There is no definite polarization direction.

edge laser with lowest threshold are shown in Figs. 14 and 15. This laser sample is the same as the one shown in the SEM picture in Fig. 2(b). The infrared camera image of the mode pattern and the polarization characteristic are shown in Fig. 14, and laser spectra and the L-L curve of this laser are presented in Fig. 15. The lattice constant of this laser sample is 1000 nm, so this laser operates near the third TE mode band edge as one can see from Fig. 13(b). Low threshold at the third band edge in 2D structures has also been predicted in theoretical works [28,29]. This originates from the fact that the higher bands are much flatter near band edges than the first band edge, which results in more enhanced density of photon states at higher band edges compared to the first band edge.

A vertical-emitting circular mode pattern observed in this laser is shown in Fig. 14(a). The hexagonal boundary of the band edge laser pattern is drawn for reference. The position of the laser emission spot is identical to the pumping position. One interesting feature is that the emission spot size is only about 2.5 μm. Remembering that the pump spot size is about 6 μm, this band edge laser seems to show nearly diffraction limited vertical emission [43]. This laser does not have a definite polarization direction as shown in Fig. 14(b), which indicates that lasing oscillations in several in-plane directions are involved in this band edge laser [23,25]. In the triangular lattice, for example, there are three equivalent directions along the Γ-M direction and also along the Γ-K direction.

The spectrum of this laser is shown in Fig. 15(a) when the incident peak pump power is 1 mW. This laser operates as a single mode in a wide spectral range, 1400 nm to 1500 nm. Output power measured

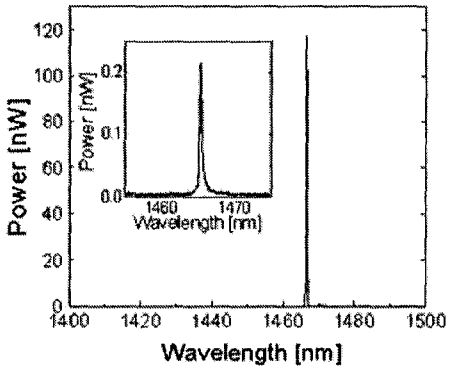

(a)

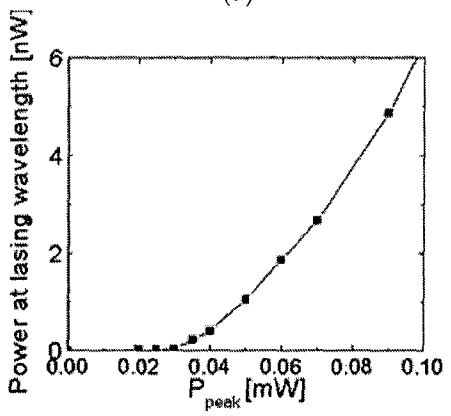

(b)

FIG. 15. Characteristics of the lowest-threshold band edge laser. (a) Spectrum when the incident peak power is 1 mW. Inset shows a spectrum when the incident pump power is 0.035 mW. (b) Collected power at the lasing wavelength is plotted as a function of incident peak pump power.

at the lasing wavelength is plotted as a function of incident peak pump power in Fig. 15(b). Laser threshold exists at the peak pump power of around 35 μW . The spectrum at this pump power is shown in the inset of Fig. 15(a). The spectral line width is nearly limited by the resolution of the optical spectrum analyzer, ~0.2 nm. The density of threshold pump power absorbed in quantum wells is estimated to be about 25 W/cm^2 assuming 20% absorption of incident power in the quantum wells. This threshold power and power density is one of the lowest values of ever reported for semiconductor lasers at this temperature [44,45]. Note that the absorbed pump power per quantum well is only 1 μW. In terms of electrical pumping, this absorbed threshold value corresponds to less than 1 μA per quantum well. The threshold carrier density is estimated to be about 5×10^{17} cm^{-3}. The transparent carrier density of the active medium is calculated based on the model in the reference [46]. It turns out that the transparent carrier density is almost the same

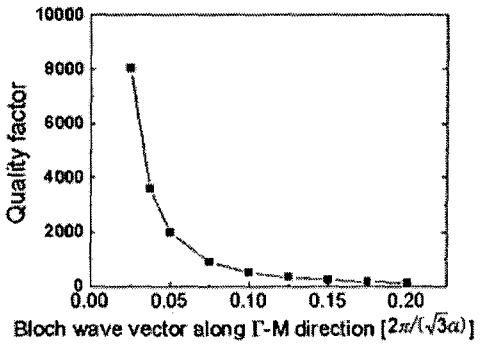

FIG. 16. Quality factors of the third TE mode calculated by the 3D FDTD method. Quality factors are plotted along the Γ-M direction of the band structure. Slab thickness and air-hole radius are 0.35 a and 0.2 a, respectively. The horizontal axis value is expressed in the unit of the M-point Bloch wave vector ($2\pi/\sqrt{3}a$).

as the threshold carrier density. This means that the threshold of this laser is nearly limited by the transparency condition, so carrier and optical losses will be very small.

The optical loss of this low threshold laser is investigated. The in-plane propagation loss of this band edge laser will be small due to the much reduced group velocity near band edges especially for the large-Δn slab. The vertical emitting characteristic also indicates that the optical loss of this laser is mainly limited by the vertical coupling loss. The vertical loss is also expected to be small because there is essentially no optical loss at the exact Γ point of certain bands [42]. This is because of the symmetry mismatch between the mode pattern at this point and free space modes. To define a true Γ point, however, one has to consider an infinite 2D photonic crystal. If the band edge lasing is observed from a finite region, the laser mode should contain non-zero k components.

The quality factor (Q) near the third TE band edge is calculated along the Γ-M direction by using the 3D FDTD method and is plotted in Fig. 16. The parameters used in this calculation are the same as those used in Fig. 15. At the Γ point, the Q is infinite, indicating no optical loss in the exact normal direction. At small k values near the Γ point, the Q is very high. It is still higher than 2000 when the k is less than 0.05 times the M point ($2\pi/\sqrt{3}a$). This k value roughly corresponds to the amount of uncertainty of the wave vector when the real space pump area is 6 μm and lattice constant is 1000 nm. Note that the pump area contains only ~30 unit cells of the photonic crystal pattern. Assuming the in-plane optical loss is much smaller than the vertical loss, this Q value can be accepted as the lower bound of the Q of the laser mode. The Q of

~2000 is similar to or larger than that of the dipole mode of the reported triangular photonic crystal single cell lasers [13,16]. In this sense, the optical loss of the free-standing photonic band edge lasers can be very small, which contributed the very low- threshold lasing action. By realizing room-temperature lasing action, the photonic band edge laser will attract great interest as a new-type of low-threshold micro-laser.

V. CONCLUSION

Low threshold lasing actions are demonstrated from free-standing photonic crystal slab structures with InGaAsP quantum-well active materials emitting at communication wavelengths. By employing a new-type of photonic crystal geometries, very low threshold which can be seen as the record values are achieved.

In the square lattice photonic crystal slab single-cell nano-cavity, a new class of two-dimensional resonant mode is found, which has the characteristics of the lowest-order whispering gallery mode. This novel resonant mode has a theoretical Q >30000 and the Purcell factor >10000. Room-temperature lasing actions are achieved from this mode with low threshold pump power of 0.8 mW. It is expected that this laser will be able to operate with threshold of $\sim 1\mu$A by improving the laser structure and the active medium.

In addition to the single-cell laser, photonic band edge lasers are realized at 80 K. The lasers operate near several photonic band edges of the free-standing photonic crystal slab. Very low threshold pump power of $\sim 35\mu$W with 6-μm pump area has been achieved in the photonic crystal laser operating at the third TE mode band edge. The low threshold operation is attributed to the low surface recombination carrier losses and increased material gain at low temperature and low optical losses near the Γ point of the photonic band.

Demonstrated photonic crystal lasers will find potential applications to nearly zero-threshold semiconductor lasers and miniaturized photonic integrated circuits.

ACKNOWLEDGEMENT

The authors appreciate valuable assistance from Dr. Jeong-Ki Hwang, Dr. Jun Huh, and Yong-Jae Lee for the FDTD calculation. The authors would like to thank Jeong-Soo Kim for his supply of the wafer. This work was supported by the National Research Laboratory Project of Korea.

*Corresponding author : hyryu@mail.kaist.ac.kr.

REFERENCES

[1] H. Yokoyama, Science **256**, 66 (1992).
[2] R. E. Slusher, Opt. & Photon. News, Feb. 8 (1993).
[3] P. L. Gourley, Nature (London) **371**, 571 (1994).
[4] R. M. De La Rue and C. Smith, Nature (London) **408**, 653 (2000).
[5] J. L. Jewell, J. P. Harbison, A. Scherer, Y. H. Lee, and L. T. Florez, IEEE. J. Quantum Electron. **27**, 1332 (1996).
[6] S. L. McCall, A. F. J. Levi, R. E. Slusher, S. J. Pearton, and R. A. Logan, Appl. Phys. Lett. **60**, 289 (1992).
[7] T. Baba, IEEE J. Selected Topics in Quantum Electron. **3**, 808 (1997).
[8] E. Yablonovitch, J. Opt. Soc. Am. B **10**, 283 (1993).
[9] J. D. Joannopoulos, P. R. Villeneuve, and S. Fan, Nature (London) **386**, 143 (1997).
[10] T. F. Krauss and R. M. D. L. Rue, Progress in Quantum Electron. **23**, 51 (1999).
[11] E. Yablonovitch, Phys. Rev. Lett. **58**, 2059 (1987).
[12] P. R. Villeneuve, S. Fan, S. G. Johnson, and J. D. Joannopoulos, IEE Proc.-Optoelectron. **145**, 384 (1998).
[13] O. Painter, J. Vučković, and A. Scherer, J. Opt. Soc. Am. B **16**, 276 (1999).
[14] J. Vučković, O. Painter, Y. Xu, A. Yariv, and A. Scherer, IEEE J. Quantum Electron. **35**, 1168 (1999).
[15] O. Painter, R. K. Lee, A. Scherer, A. Yariv, J. D. O'Brien, P. D. Dapkus, and I. Kim, Science **284**, 1819 (1999).
[16] O. J. Painter, A. Husain, A. Scherer, J. D. O'Brien, I. Kim, and P. D. Dapkus, J. Lightwave Technol. **17**, 2082 (1999).
[17] J. K. Hwang, H. Y. Ryu, D. S. Song, I. Y. Han, H. W. Song, H. K. Park, Y. H. Lee, and D. H. Jang, Appl. Phys. Lett. **76**, 2982 (2000).
[18] J. K. Hwang, H. Y. Ryu, D. S. Song, I. Y. Han, H. K. Park, D. H. Jang, and Y. H. Lee, IEEE Photon. Technol. Lett. **12**, 1295 (2000).
[19] H. G. Park, J. K. Hwang, J. Huh, H. Y. Ryu, Y. H. Lee, and J. S. Kim, Appl. Phys. Lett. **79**, 3032 (2001).
[20] H. Y. Ryu, S. H. Kim, H. G. Park, J. K. Hwang, Y. H. Lee, and J. S. Kim, Appl. Phys. Lett. (to appear in May 2002).
[21] H. Y. Ryu, S. H. Kwon, Y. J. Lee, Y. H. Lee, and J. S. Kim, Appl. Phys. Lett. (to appear in May 2002).
[22] Y. H. Lee and H. Y. Ryu, IEEE Circuits and Devices Magazine (to appear in May 2002).
[23] M. Imada, S. Noda, A. Chutinan, T. Tokuda, M. Murata, and G. Sasaki, Appl. Phys. Lett. **75**, 316 (1999).
[24] M. Meier, A. Mekis, A. Dodabalapur, A. Timko, R. E. Slusher, J. D. Joannopoulos, and O. Nalamasu, Appl. Phys. Lett. **74**, 7 (1999).
[25] M. Notomi, H. Suzuki, and T. Tamamura, Appl. Phys. Lett. **78**, 1325 (2001).
[26] A. Mekis, M. Meier, A. Dodabalapur, R. E. Slusher, and J. D. Joannopoulos, Appl. Phys. A **69**, 111 (1999).

[27] S. Noda, M. Yokoyama, M. Imada, A. Chutinan, and M. Mochizuki, Science **293**, 1123 (2001).
[28] N. Susa, J. Appl. Phys. **89**, 815 (2001).
[29] K. Sakoda, Opt. Express **4**, 167 (1999); K. Sakoda, K. Ohtaka, and T. Ueta, *ibid* **4**, 481 (1999).
[30] H. Kogelnik and C. V. Shank, J. Appl. Phys. **43**, 2327 (1972).
[31] S. G. Johnson, S. Fan, P. R. Villeneuve, and J. D. Joannopoulos, Phys. Rev. B **60**, 5751 (1999).
[32] H. Y. Ryu, J. K. Hwang, and Y. H. Lee, J. Appl. Phys. **88**, 4941 (2000).
[33] A. Taflove, *Computational electrodynamics: The finite-difference time-domain method*(Norwood, MA: Artech house, 1995).
[34] S. G. Johnson, S. Fan, A. Mekis, and J. D. Joannopoulos, Appl. Phys. Lett. **78**, 3388 (2001).
[35] J. D. Jackson, *Classical Electrodynamics* (New York: Wiley, 1999) vol. 3.
[36] T. D. Lee, P. H. Cheng, J. S. Pan, R. S. Tsai, Y. Lai, and K. Tai, Appl. Phys. Lett. **72**, 2223 (1998).
[37] S. Haroche and D. Kleppner, Phys. Today, Jan. 24 (1989).
[38] J. M. Gerard and B. Gayral, J. Lightwave Technol. **17**, 2089 (1999).
[39] A. Scherer, O. Painter, B. D'Urso, R. Lee, and A. Yariv, J. Vac. Sci. Technol. B **16**, 3906 (1997).
[40] H. Y. Ryu, Y. H. Lee, R. Sellin, and D. Bimberg, Appl. Phys. Lett **79**, 3573 (2001).
[41] A. Chutinan and S. Noda, Phys. Rev. B **62**, 4488 (2000).
[42] T. Ochiai and K. Sakoda, Phys. Rev. B **63**, 125107 (2001).
[43] S. Riechel, C. Kallinger, U. Lemmer, J. Feldmann, A. Gombert, V. Wittwer, and U. Scherf, Appl. Phys. Lett. **77**, 2310 (2000).
[44] H. Cao, J. Y. Xu, W. H. Xiang, Y. Ma, S. H. Chang, S. T. Ho, and G. S. Solomon, Appl. Phys. Lett. **76**, 3519 (2000).
[45] R. E. Slusher, A. F. J. Levi, U. Mohideen, S. L. McCall, S. J. Pearton, and R. A. Logan, Appl. Phys. Lett. **63**, 1310 (1993).
[46] L. A. Coldren and S. W. Corzine, *Diode lasers and photonic integrated circuits*, (New York, NJ: John Wiley & Sons, 1995).